
ACCELERATED HYDRATION SITE LOCALIZATION AND THERMODYNAMIC PROFILING

A PREPRINT

Florian B. Hinz ^{*†‡} Matthew R. Masters ^{*†‡} Julia N. Kieu ^{*} Amr H. Mahmoud ^{*†} Markus A. Lill ^{*†§}

November 26, 2024

ABSTRACT

Water plays a fundamental role in the structure and function of proteins and other biomolecules. The thermodynamic profile of water molecules surrounding a protein are critical for ligand binding and recognition. Therefore, identifying the location and thermodynamic behavior of relevant water molecules is important for generating and optimizing lead compounds for affinity and selectivity to a given target. Computational methods have been developed to identify these hydration sites, but are largely limited to simplified models that fail to capture multi-body interactions, or dynamics-based methods that rely on extensive sampling. Here we present a method for fast and accurate localization and thermodynamic profiling of hydration sites for protein structures. The method is based on a geometric deep neural network trained on a large, novel dataset of explicit water molecular dynamics simulations. We confirm the accuracy and robustness of our model on experimental data and demonstrate its utility on several case studies.

1 Introduction

Water plays a fundamental role in the structure and function of proteins and other biomolecules. The ubiquitous presence of water in protein environments significantly impacts the stability, dynamics, and interactions with other molecules. In particular, the desolvation of hydrophobic moieties is known to be a major driving force for ligand binding and recognition. Water molecules may also mediate interactions between ligand and protein, through the formation of water bridges. Therefore, a complete understanding of the effect of solvation is essential to optimize the binding affinity and selectivity of lead compounds. Beyond small molecules, water also plays an important role in mediating other interactions such as protein-protein and other biomolecular interactions, which are becoming increasingly important with the development of new biologic products.

Due to its importance and range of potential applications, numerous computational methods have been developed in order to predict the location of hydration sites, localized regions of high water density. However, these methods are usually limited to simplified models that fail to capture the dynamic behavior and multi-body interactions inherent in water networks, or dynamics-based methods that rely on extensive sampling that is computationally prohibitive for flexible proteins with significant conformational change. Furthermore, simply identifying the position of likely water molecules is insufficient for ligand optimization since the thermodynamic profile of individual water molecules dictates whether displacement by a ligand is energetically favorable or not. Computational methods also exist for estimating the thermodynamic properties of hydration sites but suffer from the same accuracy/cost trade-off between static and dynamic-based methods.

^{*}Department of Pharmaceutical Sciences, University of Basel, Basel, Switzerland

[†]Swiss Institute of Bioinformatics, Basel, Switzerland

[‡]These authors contributed equally to this work.

[§]Corresponding Author: markus.lill@unibas.ch

In this paper, we introduce a generative deep learning model that is capable of fast and accurate hydration site identification and thermodynamic profiling. Unlike previous methods, our model is capable of predicting hydration sites in one-shot with near dynamics-level accuracy. The model is able to resolve complex multi-body interactions in a fixed-time and propose physically valid water networks along with associated enthalpic and entropic contributions. It is based on an equivariant transformer network and is trained to match the explicit distribution of hydration sites on a protein surface. Training was done using a novel dataset of WATsite simulation results from thousands of diverse protein systems, representing a high level of robustness and generalizability across protein space. Our method was validated using a difficult hold-out set of unseen protein sequences in addition to high-quality crystallographic waters. We further demonstrate and discuss our model’s utility on a number of interesting drug and protein design scenarios.

2 Background and Related Methods

2.1 Experimental Determination

Water locations can be resolved using several experimental methods including x-ray/neutron crystallography [1], cryo-EM [2, 3], and NMR [4]. Crystallography is the most common technique with more than half of the experimental structures containing at least one water molecule [5]. However, there are a number of technical challenges associated with the determination of water locations leading to certain limitations. Most of these challenges arise from the complex multi-body interactions and high mobility inherent to water molecules. Experimental determination is often limited to the first shell of waters, especially on the solvent-exposed surface and not buried within the protein. Furthermore, experimental approaches have limited resolution and water positions often have non-ideal interaction geometry. Lastly, experimental determination of water locations does not quantify thermodynamics properties such as enthalpy and entropy.

2.2 Computational Methods

While experimental determination of water structure is indispensable for providing the ground truth, they are limited by real-world constraints such as time, cost, and technical feasibility. To overcome these challenges, a number of computational methods have been developed to predict the location of water molecules around an existing protein structure. These methods can be largely grouped into two categories, static and dynamic. Static methods assume the water network has a constant position and neglects any slowly-resolving water-water or water-protein interactions as well as any protein movement or flexibility. Among the static methods, most fall into the category of knowledge-based, such as 3D-RISM [6, 7, 8], AQUARIUS [9], SZMAP [10], and WaterFLAP [8, 11, 12], geometry-based, such as AcquaAlta [13], Auto-SOL [14], HADDOCK [15], WarPP [16], and WATGEN [17], or energy-based, such as Fold-X [18] or WaterDock [19].

Dynamic methods often employ molecular dynamics (MD) simulations which utilize an explicit water model and protein force field. By using MD simulations, one can generate a trajectory detailing the atomic behavior of water with other molecules in solution. This trajectory can be later analyzed to identify regions of high water density, characterize the thermodynamics of these sites, and understand detailed interactions involving water. However, the limitation of dynamic methods is that they are computationally and time intensive, especially due to the calculation of large number of non-bonded interactions that is required by the explicit water simulation. Furthermore, in order to ensure convergence of the water density within a reasonable time, strong positional constraints are added to the protein solute, removing any flexibility and perturbation to the initial protein structure [20, 21]. While these constrained results can still be useful in guiding structure-based drug design for particular targets, we know that protein flexibility plays a significant role in most drug targets and that even small perturbations to protein structure can lead to drastically different hydration shell structure [22]. Therefore, dynamic methods are still largely limited to single protein structures and require either multiple runs or time-consuming, extensive runs in order to achieve proper convergence. Among the dynamic methods are HydraMap [23], HyPred [24], MobyWat [25, 26], WaterMap [27, 8], and WATsite [28, 29, 30].

More recently, some works have employed machine learning and deep neural networks towards the prediction of hydration shell structure. For example, several groups have used convolutional neural networks that work on 3D grids in order to predict the water density such as GalaxyWater-CNN [31], HydraProt [32], and Ghanbarpour et al., 2020 [33]. In another work, Park developed a SE(3)-equivariant network that is capable of directly predicting positions of water molecules given pre-defined probe locations [34]. Lastly, SuperWater is a diffusion-based model designed to generate crystal waters given the protein structure [35]. While these methods take a step towards the development of a one-shot hydration site predictor, they still fall short by either training on sparse and poorly modeled crystallographic data or by not considering the thermodynamic contributions of hydration sites.

3 Methods

The prediction of the hydration sites with associated thermodynamic properties consists of two separate models. The first model predicts the hydration site location and is explained in section 3.1. The predicted coordinates then serve as an input to the second model, which predicts the associated entropy and enthalpy values (see section 3.2). The code and a reference to the training data are provided at <https://github.com/lillgroup/HydrationSitePrediction>.

3.1 Location prediction

The procedure of learning the hydration site locations is inspired by our previous work [36] and schematically shown in Figure 1. The input data consists of the atom coordinates and the associated feature vectors. The feature vector is 92 dimensional consisting of a one-hot encoding of the atom type (38 dimensions), a one-hot encoding of the residue type (21 dimensions), a radial basis function expansion of the SASA value (32 dimensions) and a one-hot encoding for the node type (atom or predicted water, 1 dimension). Initially, $n \in \mathbb{N}$ water predictions are placed at the position of any atom of a SASA value greater than 0.1 (see Figure 1A). A graph structure is constructed from the atom positions by connecting any two nodes (i.e. atoms) via an edge, if their distance is less than 6Å. The edge feature encoding consists of a radial basis function expansion of the edge length (32 dimensions). We apply a first equivariant attention layer to the graph structure to obtain updated locations of the water molecule nodes. The protein atom positions are left unchanged. The graph topology is updated by also including the nodes representing the water molecules and again constructing edges between nodes less than 6 Å apart. Five equivariant attention layers are applied to perturb the nodes representing water molecules, with the distance-based graph topology being updated before applying each layer (see B and C in Figure 1). The network is trained by minimizing a loss function that resembles the Kullback-Leibler divergence between two gaussian mixture models: Once the mixture components are defined via the ground truth water coordinates and once via the predicted coordinates. Details about the loss function are provided in the following paragraph.

3.1.1 Loss function

The equivariant graph neural network as discussed in section 3.1 outputs tuples $(x_j, w_j) \in \mathbb{R}^3 \times [0, 1]$ for $j \in \{1, \dots, n\}$ and $n \in \mathbb{N}$ the number of initially placed water prediction nodes. The first element $x_j \in \mathbb{R}^3$ represents the coordinates of the predicted hydration site (see D in Figure 1), while $w_j \in [0, 1]$ corresponds to an associated certainty weight of the prediction. Defining for $j \in \{1, \dots, n\}$ the normalized certainty weights as

$$q_j := \frac{w_j}{\sum_{i=1}^n w_i}, \quad (1)$$

we consider the tuples $((x_j, q_j))_{j=1}^n$ as a representation of components of a Gaussian mixture distribution as follows:

$$q(x) := \sum_{j=1}^n q_j \frac{1}{\sqrt{(2\pi)^3} \sigma^3} \exp\left(-\frac{1}{2\sigma^2} \|x - x_j\|_2^2\right), \quad (2)$$

where the standard deviation is chosen as $\sigma = 0.5$. For a given protein in the training set, let us denote the true $m \in \mathbb{N}$ hydration sites with associated occupancies of at least 0.5 as tuples (u_j, o_j) for $j \in \{1, \dots, m\}$. Similarly as in 1 and 2 we define

$$p_j := \frac{o_j}{\sum_{i=1}^m o_i}, \quad (3)$$

and consider the true hydration sites representing a Gaussian mixture distribution as follows

$$p(x) := \sum_{j=1}^m p_j \frac{1}{\sqrt{(2\pi)^3} \sigma^3} \exp\left(-\frac{1}{2\sigma^2} \|x - u_j\|_2^2\right). \quad (4)$$

As a simplified surrogate for the symmetrized Kullback-Leibler divergence $\text{KL}(p|q) + \text{KL}(q|p)$, we choose

$$L_1\left(\left((x_j, q_j)\right)_{j=1}^n, \left((u_j, p_j)\right)_{j=1}^m\right) := \sum_{j=1}^m p_j \log\left(\frac{p_j}{q(u_j)}\right) + \sum_{j=1}^n q_j \log\left(\frac{q_j}{p(x_j)}\right). \quad (5)$$

We found it beneficial to introduce a further loss term, penalizing the concentration of weights:

$$L_2((q)_{j=1}^n) := \sum_{j=1}^n q_j^2. \quad (6)$$

The total loss function consists of a weighted sum of L_1 and L_2 :

$$L_3 \left(((x_j, q_j)_{j=1}^n), ((u_j, p_j)_{j=1}^m) \right) = L_1 \left(((x_j, q_j)_{j=1}^n), ((u_j, p_j)_{j=1}^m) \right) + \alpha \cdot L_2 \left((q)_{j=1}^n \right),$$

for some hyperparameter $\alpha > 0$.

3.1.2 Clustering

At inference time, we first filter out predictions with certainty weights lower than a cutoff $w_c = 0.035$. To the remaining predictions we apply an agglomerative clustering as implemented in [37] with a linkage distance threshold of 2\AA to end up at well separated predictions (see E in Figure 1). Let $M, k, k_1, \dots, k_M \in \mathbb{N}$ and

$$C_k = \{(x_{k_1}, w_{k_1}), \dots, (x_{k_M}, w_{k_M})\},$$

be the k 'th cluster determined by the algorithm. We define the weighted cluster mean with associated certainty weight as

$$(x_{C_k}, w_{C_k}) = \left(\sum_{j=1}^M w_{k_j} x_{k_j}, \sum_{j=1}^M w_{k_j} \right).$$

We consider $x_{C_k} \in \mathbb{R}^3$ a predicted hydration site location (see 1D) if the associated certainty weight w_{C_k} exceeds a threshold of 0.1.

3.2 Entropy and enthalpy prediction

Figure 2 schematically shows the learning of the entropy and enthalpy values of each hydration site. First, a graph is constructed with nodes representing atoms and hydration sites. During training, true hydration sites from WATsite with occupancy values greater than 0.3 are considered nodes. The edges are constructed based on a distance cutoff of 8\AA , ignoring intramolecular edges within the protein. The feature vectors associated with the nodes are similarly constructed as for the location prediction model (see section 3.1). The feature vectors are updated by applying three layers of a graph attention network as introduced in [38] (see Figure 2 B). A feed forward network is applied to each feature vector to end up at a 2 dimensional output representing entropy and enthalpy (see Figure 2 C). The loss function during training consists of the sum of the mean squared errors of entropy and enthalpy over all hydration sites with occupancy of at least 0.5:

$$L_{\text{thermo}} \left((\hat{E}_i, E_i)_{i=1}^n, (\hat{S}_i, S_i)_{i=1}^n \right) = \frac{1}{n} \sum_i \left(E_i - \hat{E}_i \right)^2 + \left(S_i - \hat{S}_i \right)^2,$$

where $n \in \mathbb{N}$ is the number of hydration sites with occupancy of at least 0.5 and \hat{E}_i denotes the model prediction for the target value enthalpy E_i for the hydration site $i \in \{1, \dots, n\}$. Similarly, the prediction of the target value entropy S_i is denoted by \hat{S}_i for $\{1, \dots, n\}$.

3.3 Dataset

The training data was prepared using WATsite [28, 39] and the number of proteins contained in the dataset was 4148, with occupancy and thermodynamic values for the HS. For the selection of the dataset, 19443 proteins from PDBbind [40, 41] were grouped by their UniProt ID and one representative structure was randomly picked from the group to prevent redundancy. The test set was selected to be as different from the validation and train set as possible, to evaluate the model's ability to generalize new targets. This was done with the sequence-similarity-based splitting strategy, in which the pairwise sequence similarity of all proteins was computed by MMSeqs2 [42] and all PDBs up to a certain similarity threshold were grouped together. The similarity cutoff in this case was 35 % and splitting was done until a 75:25 train test ratio was achieved. Ultimately, the train set contained 2766 proteins, the test set contained 1083 proteins, and the validation set contained 305 proteins.

For the MD simulation the co-crystallized small molecules, waters and ions were removed with Schrödinger's Protein Preparation Wizard [43]. Simulations were performed with Schrödinger's Desmond according to its standard NPT relaxation protocol [44]. The production simulations ran at 300K for 20 ns each, with a $50 \text{ kcal mol}^{-1} \text{\AA}^{-2}$ large positional restraint applied to all heavy atoms. Every 20 ps snapshots were taken, resulting in 1000 frames per simulation for analysis. Using VMD [45] the MD simulations were aligned and recentered and the hydration sites calculated from

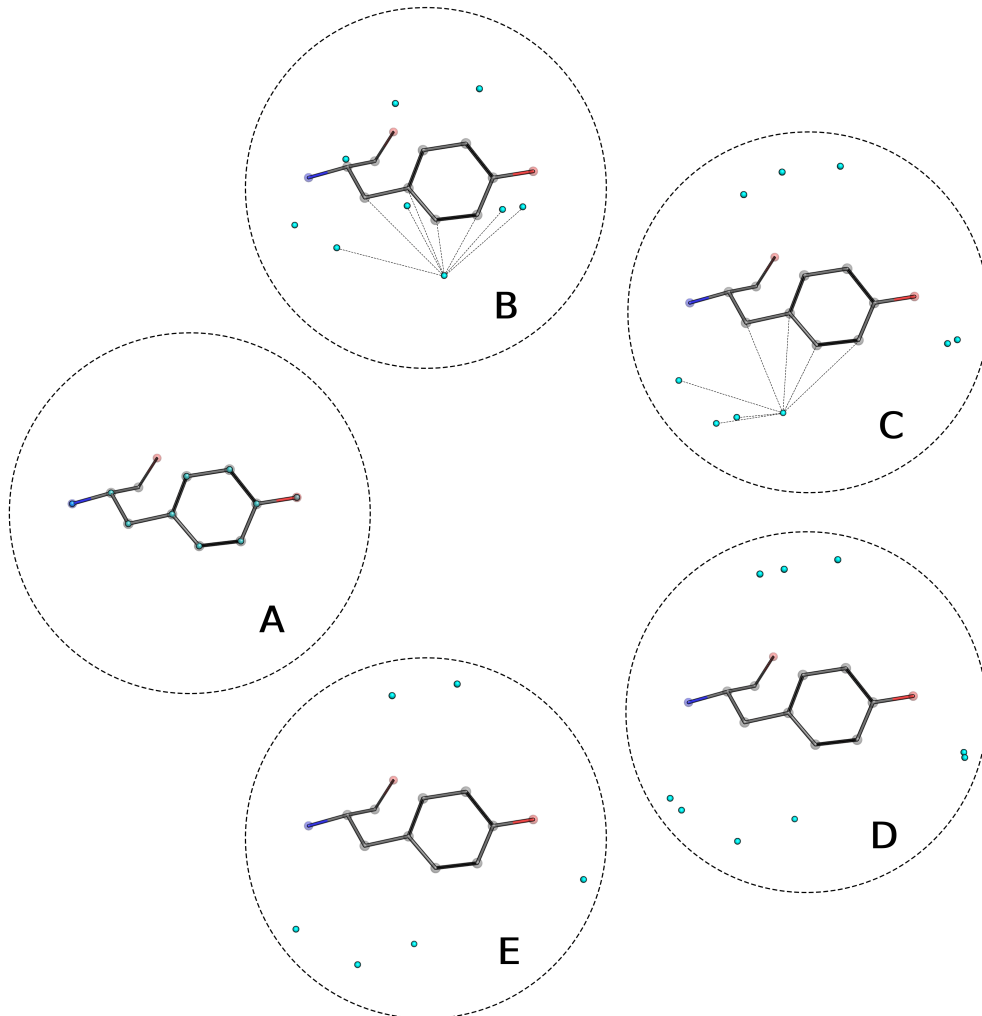


Figure 1: Schematics displaying the coordinates prediction of hydration sites. **A**: Initially, we position a water prediction (light blue spheres) at every atom exceeding a certain cutoff of solvent exposure (SASA greater than 0.1). An equivariant attention layer is applied to the distance-based graph topology to perturb the water predictions. **B, C**: The distance based graph topology is updated by now also considering water predictions as graph nodes. An equivariant attention layer perturbs the water predictions. **D**: After the application of five layers, predictions of low certainty are filtered out and a clustering algorithm is applied to end up at the final water predictions (**E**).

each simulation trajectory using the WATsite program. The water molecules were tracked throughout the simulation and their density is discretized onto a grid with resolution of 0.25\AA . A hierarchical clustering algorithm clustered the grid into hydration sites with a radius of 1\AA . Water molecules belonging to each hydration site are extracted from the simulation allowing for the calculation of thermodynamic properties. The change in enthalpy (ΔH) was determined based on the average sum of van der Waals and electrostatic interactions between each water molecule inside a hydration site with the protein and other water molecules compared to the value in bulk solvent. Meanwhile, the entropy was estimated by integration of the external mode probability density function (PDF, $p_{ext}(q)$) of the water molecules' translational and rotational motions during the MD simulation via the following formula:

$$\Delta S_{hs} = R \ln \left(\frac{C^\circ}{8\pi^2} \right) - R \int p_{ext}(q) \ln p_{ext}(q) dq \quad (7)$$

With R being the gas constant, C° the concentration of pure water ($1 \text{ molecule}/29.9 \text{\AA}^3$). From entropy and enthalpy, the Gibbs free energy of the desolvation of hydration sites could be calculated using the following formula: $\Delta G = \Delta H - T\Delta S$. It represents the temperature (T) dependent change of entropy and enthalpy of a water molecule inside a hydration site, when it is transferred from the bulk solvent into the hydration site of the protein cavity [46].

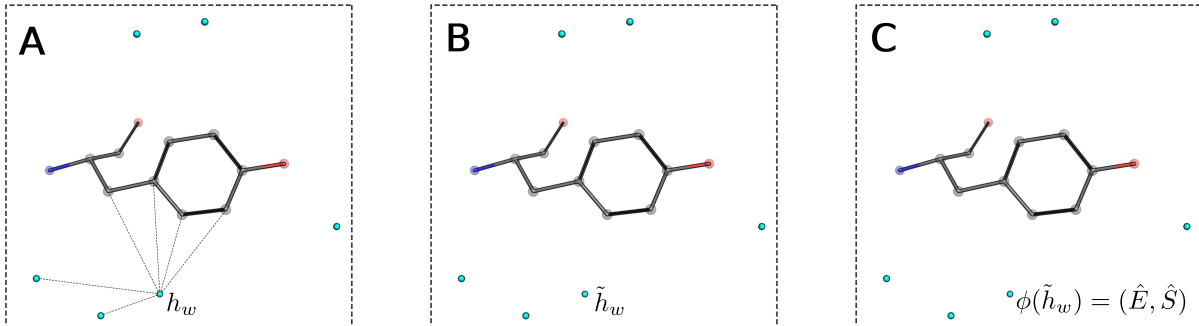


Figure 2: Schematics displaying the prediction of entropy and enthalpy. **A**: The input consists of coordinates and feature vectors for protein atoms and hydration sites. The edges are constructed based on distances. **B**: A graph attention network is applied and outputs a modified feature vector per graph node. **C**: A feed forward network is applied to the feature vectors of the water nodes. The output consists of the enthalpy and entropy values.

4 Results and Discussion

4.1 Hydration site prediction

In the following, we present the results of the model discussed in section 3.1 on the test set (similar results for the training set are given in section B.2 of the Appendix). We evaluate the prediction performance in terms of the **Ground Truth Recovery Rate (GTRR)** and **Prediction Hit Rate (PHR)** as defined in Appendix C. Table 1 shows the GTRR and PHR for a cutoff value of 0.5 Å and 1.0 Å. The model recovers 59% of the true hydration site at a cutoff level of 0.5 Å divergence. If we increase the cutoff to 1.0 Å, then 80.2% of hydration sites are recovered. On the other hand, a proportion of 48.3% of predictions is closer than 0.5 Å to a true hydration site and 65.9% are closer than 1.0 Å.

Cutoff	Ground Truth Recovery Rate	Prediction Hit Rate
0.5	59.0%	48.3%
1.0	80.2%	65.9%

Table 1: Ground truth recovery rate and prediction hit rate on WATsite test set

We consider a hydration site to be in the *first layer* if it is in no further distant than 3.5 Å from a non-hydrogen atom of the protein. Otherwise the hydration site is in the second layer. Table 2 shows the GTRR for first and second layer hydration sites at cutoff levels of 0.5 and 1.0 Å. We observe that the model very successfully predicts first layer hydration site coordinates with a GTRR of 62.5% and 84.5% for and 0.5 and 1.0 Å respectively. The second layer hydration sites are substantially more challenging to predict correctly, as only 15.2% and 26.9% of true hydration sites are recovered at a tolerance cutoff of 0.5 and 1.0 Å respectively. These results indicate a clear distinction in the model’s predictive accuracy between first and second shell hydration sites. First layer hydration sites are strongly influenced by electrostatic and steric effects, often forming direct hydrogen bonds with the protein, making them more predictable. Second layer hydration sites have reduced accuracy, like due to their weaker, indirect interactions with the proteins. This leads to greater mobility of the water and less localized water density.

Cutoff	GTRR first layer	GTRR second layer
0.5	62.5%	15.2%
1.0	84.5%	26.9%

Table 2: Ground truth recovery rate (GTRR) for first and second layer

We further investigate the recovery performance for hydration sites differentiated based on occupancy in Table 3. As one would naturally expect, the GTRR increases with higher occupancy, meaning more stable hydration sites are easier to predict. The GTRR is highest for hydration sites of an occupancy between 0.8 and 0.9 with 70.0% and 91.0% for a

divergence cutoff of 0.5 and 1.0 Å respectively. For the hydration sites of highest occupancy (between 0.9 and 1.0) the model receives almost the same performance with 69.7% and 90.8% respectively.

	Occupancy				
	[0.5,0.6]	[0.6,0.7]	[0.7,0.8]	[0.8,0.9]	[0.9,1.0]
Cutoff					
$r = 0.5$	42.1%	57.2%	65.1%	70.0%	69.7%
$r = 1.0$	62.4%	79.4%	86.9%	91.0%	90.8%
$r = 1.5$	70.4%	86.3%	92.5%	95.7%	94.4%
$r = 2.0$	75.1%	89.5%	94.8%	97.3%	95.6%

Table 3: Ground truth recovery rate at different occupancy levels

As shown in Table 4, the results significantly improve for low occupancy rates, if we just consider the hydration sites of the first layer.

	Occupancy				
	[0.5,0.6]	[0.6,0.7]	[0.7,0.8]	[0.8,0.9]	[0.9,1.0]
Cutoff					
$r = 0.5$	48.5%	60.6%	67.0%	70.9%	69.9%
$r = 1.0$	71.0%	83.6%	89.0%	91.9%	90.9%
$r = 1.5$	79.4%	90.5%	94.5%	96.5%	94.5%
$r = 2.0$	83.7%	93.3%	96.5%	97.9%	95.7%

Table 4: First layer waters: Ground truth recovery rate at different occupancy levels

4.2 Thermodynamic Profiling

In the following, we evaluate our model for thermodynamic profile prediction as introduced in section 3.2. Given the coordinates of the true hydration sites, we investigate how accurately the model can recover the enthalpy and entropy values given by the explicit-water MD simulations with WATsite. A case study where we predict thermodynamic properties based on predicted hydration site locations is provided in subsection 4.3.5.

Table 5 shows the results for both enthalpy and entropy in terms of mean squared error and Pearson correlation on the test set. The correlation for enthalpy and entropy is visualized in hexbin density plots in Figure 10 and 11 respectively. We observe that given the true hydration site coordinates, the correlation between model predictions and the corresponding simulated target values is high, with 0.864 for entropy and 0.839 for enthalpy. Interestingly, there seems to be an increasing uncertainty for predictions in the case of higher entropy values. High-entropy waters are often characterized by greater mobility, weaker structural organization and fewer hydrogen bonds. This leads to a broader distribution of possible locations and orientations of the water molecule. Consequently, these less ordered hydration sites are harder to predict accurately.

	Entropy	Enthalpy
MSE	0.218	0.38
Correlation	0.864	0.839

Table 5: Correlation and Means Squared Error (MSE) between prediction and ground truth for both entropy and enthalpy on the test set

4.3 Case Studies

In order to investigate the accuracy and behavior of the model more intently, we looked at five specific systems: Disulphide Catalyst DsbA, Triosephosphate Isomerase, Heat Shock Protein 90 (HSP90), Clarin-2, and Major Urinary

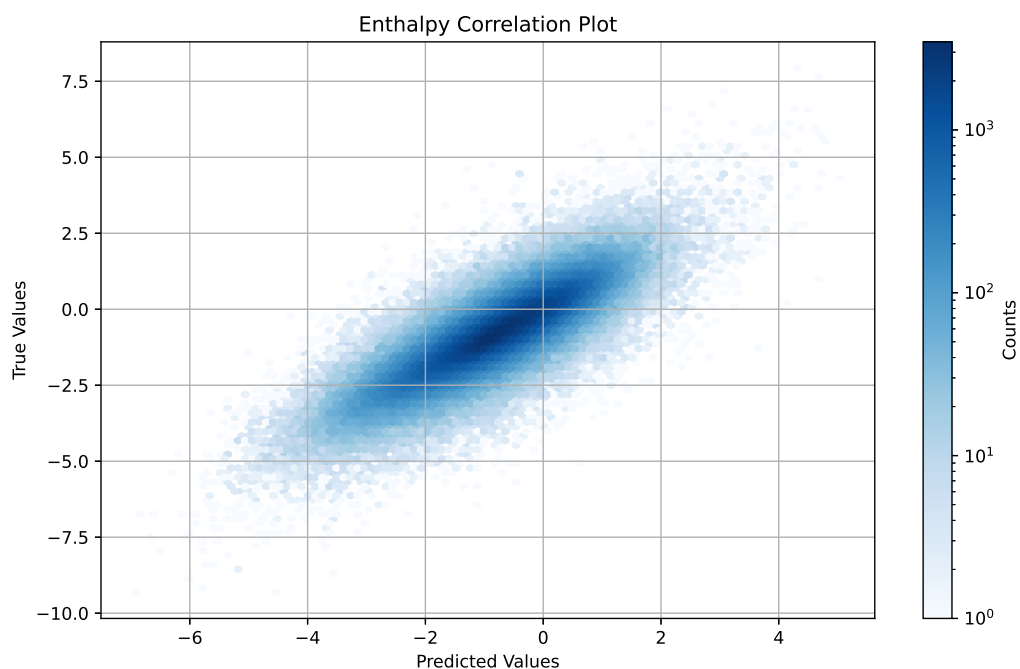


Figure 3: Hexbin plot showing the correlation between the enthalpy predictions and the enthalpy values obtained from WATsite for the test set.

Protein (MUP). The first two focus on conserved water networks important for structure and function as well as the effect of point mutations. The HSP90 example focuses on conformational changes ranging from side-chain rotation to loop reorganization. Clarin-2 was used to test the ability of the model to predict hydration information using AlphaFold3 structures of unresolved membrane-bound proteins. Finally, in the MUP case study we apply thermodynamic predictions to the case of protein-ligand binding and show that a strong correlation can be established between the estimated free energy of desolvation and experimentally measured affinity values for a series of ligands.

4.3.1 Disulphide Catalyst DsbA

Disulphide Catalyst DsbA is an important enzyme for the formation of disulphide bonds, which are present in many proteins entering the secretory pathway [47]. Importantly, disulphide catalysts contain a conserved buried water network within the active site that is essential for its function. It is believed that the water network acts as a "proton wire" that shuffles protons from the bulk solvent to the catalytic cysteine residues. Previous studies have investigated the effects of point mutations within the active site using x-ray crystallography [48]. In this experiment, we aimed to test if our model could correctly generate the conserved water network structure and respond accurately to point mutations. The results, shown in Figure 5, show a high level of accuracy for both the wild type (WT) and both point mutations (E24A and E37A). In each case, we were able to correctly identify all of the hydration sites within 1.0 Å. These results demonstrate the model is capable of predicting structurally and functionally important water networks with a high degree of accuracy. The model also appears robust and generalizable by its ability to accurately respond to point mutations. A common fault of deep-learning-based models is their tendency to overfit and inability to behave accurately outside of the training data distribution [49]. However, the results indicate our model is not overfit on any particular protein folds and can respond to small changes in protein structure. Lastly, the predicted hydration sites appear to be physically valid with no steric clashes and reasonable interatomic distances.

4.3.2 Triosephosphate Isomerase

Triosephosphate isomerase is a dimeric enzyme involved in the glycolysis pathway and is found in nearly all organisms [50]. Like in the previous case study, triosephosphate isomerase also contains a conserved water network. However, in this case the water network is present at the interface of the homodimer structure and not buried within the protein. The

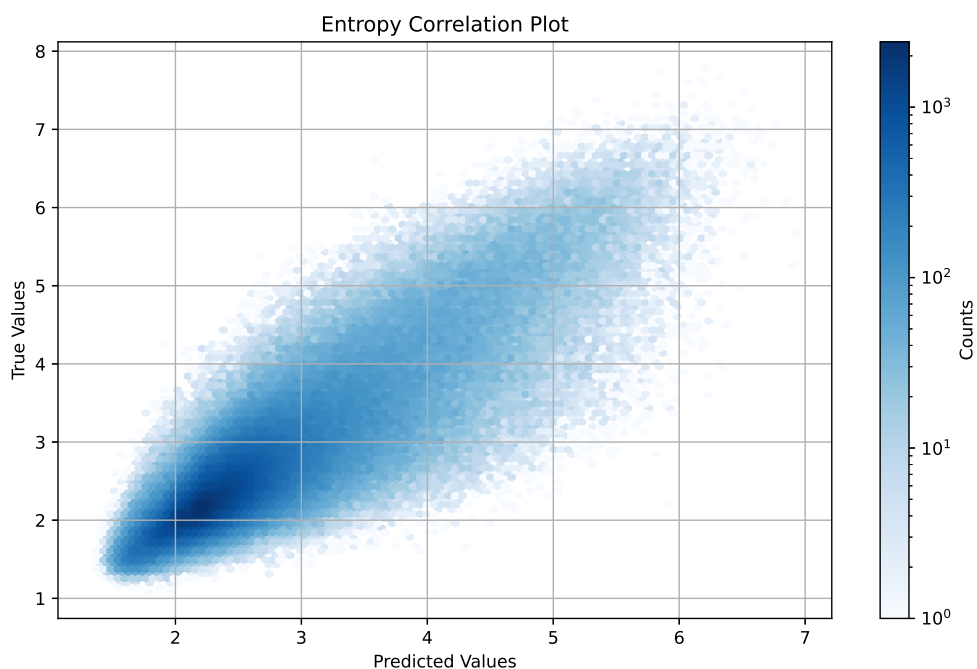


Figure 4: Hexbin plot showing the correlation between the entropy predictions and the entropy values obtained from WATsite for the test set.

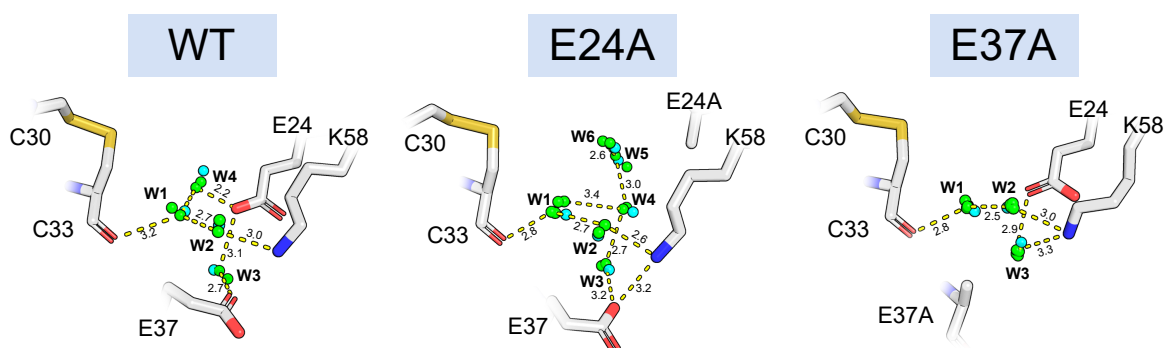


Figure 5: Buried water network important for the activity of disulphide catalyst DsbA. We evaluated the wildtype (PDB: 5QO9) as well as two mutants known to disrupt the conserved water network, E24A (PDB: 8EQR) and E37A (PDB: 8EQQ). Crystal waters are shown from all superimposed chains in green. Hydration site predictions are shown in cyan. Relevant distances are shown and labelled with their length in Angstrom. Predictions beyond the selected crystal hydration sites are not shown.

predictions showed very strong agreement with experimental data with 20/21 crystal waters predicted within 1.0 Å (Figure 6A). Upon further inspection of the single failure, our proposed hydration sites occupy unmodelled regions of electron density, potentially offering a better fit than the PDB deposited structure (Figure 6B).

4.3.3 Heat Shock Protein 90

The location of hydration sites is highly dependent on protein conformation [21, 22]. Therefore, it is essential that the model is capable of responding to changes in the protein ranging from small perturbations to large-scale conformational changes. To this end, we predicted hydration sites for HSP90 in two conformations which exhibits both small and large conformational change (Figure 7). In regions where the conformation is similar, the model predicted similar

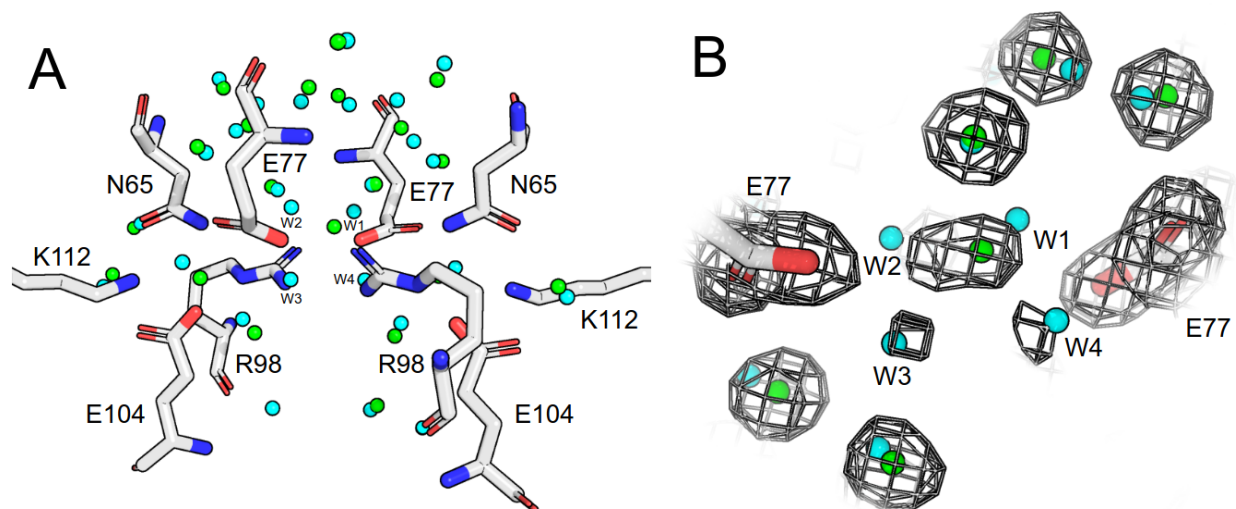


Figure 6: Conserved water network at the dimer interface of triosephosphate isomerase. A) Residues at interface of subunits A (right) and B (left) with crystal waters (green) and predicted hydration sites (cyan). B) Focused view of the single failure at center of interface with $2fo-fc$ map shown as mesh with isovalue of 1.0.

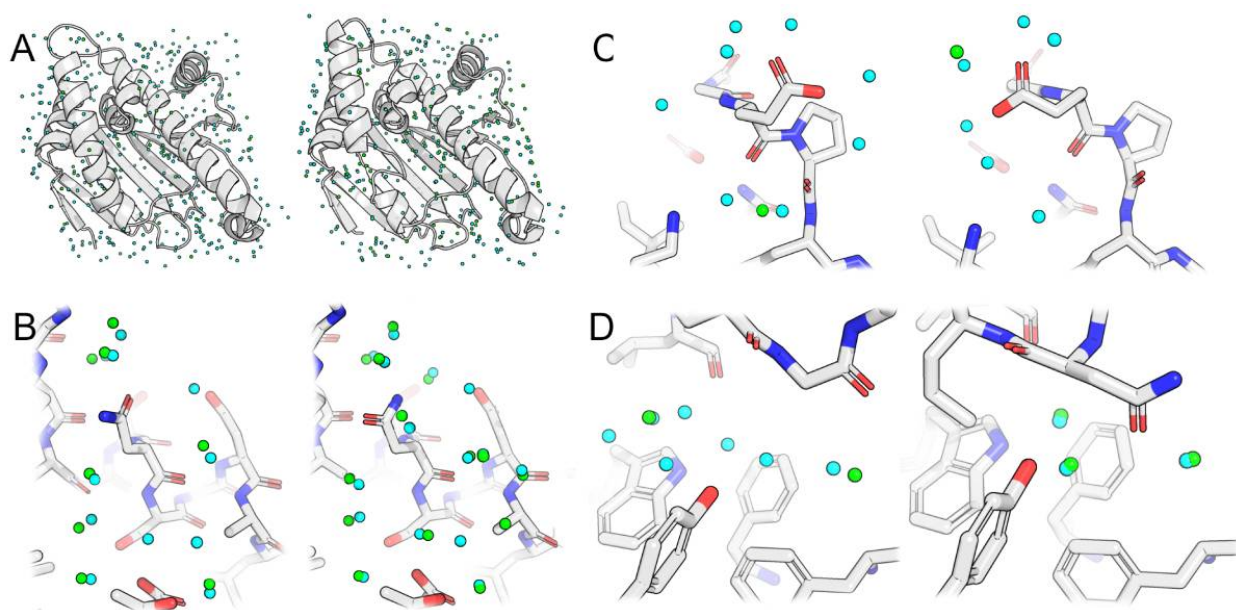


Figure 7: Comparison of HSP90 in two conformations from PDBs 2QFO and 2WI7 on the left and right respectively. A) Full protein structures with all crystal waters (green) and predictions (cyan). B) Focused view on region with similar conformation in both structures and strong agreement with crystal waters. C) Example of flexible side-chain in different conformations with corresponding predicted waters. D) Several hydration sites occupying the open pocket of 2QFO are displaced or stabilized by the α -helix3 side-chains seen in the 2WI7 loop-in structure.

water networks that exhibited strong agreement with crystal water locations (Figure 7B). This confirms that distant changes in protein structure does not result in undue changes to the hydration site prediction. In the case of a flexible side-chain that can adopt multiple possible conformations, the model was able to adapt to the change, maintaining proper hydrogen bond distances and avoiding steric clashes (Figure 7C). This finding demonstrates the robustness of our model in responding to small changes and accurately modelling atomic interactions. This also shows that our model is not overfit to any particular conformation and the network hasn't simply memorized the placement of hydration sites based on sequence alone. HSP90 also exhibits a larger conformational change among its α -helix3. In 2QFO the α -helix is intact while in 2WI7 the helix unfolds in the middle and adopts a "loop-in" conformation. The model

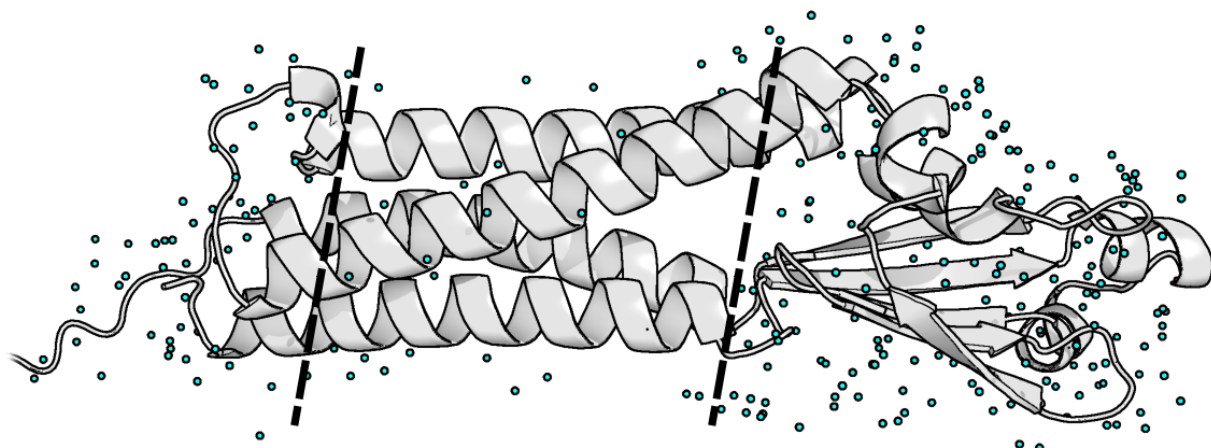


Figure 8: Hydration site predictions for membrane-bound protein Clarin-2 generated via AlphaFold3. The predictions show that they are robust to different molecular environments and can accurately predict the number of waters depending on the environment. In the hydrophobic, membrane-bound core of the protein, there are very few predicted waters. However, the hydrophilic intra- and extra-cellular sides had a large number of predicted sites.

accurately responds to the large conformational change and is able to detect both the displacement and stabilization of several sites, further supported by crystallographic waters (Figure 7D).

4.3.4 Clarin-2

One exciting new opportunity to test our model is on the host of computationally predicted structures which have not been experimentally determined. This is especially interesting since leading protein structure methods, such as AlphaFold3 and RosettaFold-AllAtom, do not consider water molecules in their predictions [51, 52]. Thus, there exists thousands of protein structures for which important water locations cannot be predicted easily. To demonstrate this advantage, we used AlphaFold3 to predict the structure of a membrane-bound protein Clarin-2, which has no structure contained in the PDB. The structure of membrane-bound proteins are often difficult in general to predict due to their inability to crystallize, although recent advances have enabled the determination of some membrane-bound proteins [53, 54]. The Clarin-2 protein is essential for hearing function by maintaining stereocilia integrity and could have therapeutic applications [55, 56]. The AlphaFold3 structure seems reasonable according to the confidence metrics and visual inspection; the structure contains the expected four transmembrane domains as well as interfaces on the intra and extra-cellular sides [57]. An interesting finding was observed after predicting the water locations, shown in Figure 8. A clear distinction in the number of predicted waters can be seen between the exposed intra/extra-cellular regions and the membrane-bound region. This result demonstrates the ability of our model to not only accurately predict the locations of waters surrounding a protein but to also accurately predict their likelihood. Furthermore, it shows that the model is able to capture essential aspects of physics such as hydrophobicity.

4.3.5 Major Urinary Protein (MUP)

The free energy of desolvation is a major driving force for protein-ligand binding. In order to test the performance of our thermodynamic profiling in the context of ligand binding, 12 cocrystallized ligands to MUP were overlaid with the predicted hydration sites and the free energy of desolvation was calculated based on the displaced water molecules (Table 6)¹

While the desolvation free energy is only one component of ligand binding, these ligands are largely hydrophobic and share a single carboxylic acid moiety, and therefore the predominant difference between them is the number and position of displaced water molecules. Figure 9 shows a regression plot between the predicted energies¹ for all ligands in the data set and the experimentally measured values. At a water displacement tolerance level of 2.4 Å, we obtain a Pearson R correlation of 0.930.

¹Shown are the transformed predictions obtained by a linear regression of the experimental values on the model predictions.

PDB ID	1ZND	1ZNE	1ZNG	1ZNH	1ZNK	1QY1	1QY2	1I06	1I06	1I06	1I06	1I06
Ligand	PE9	HE2	HE4	OC9	F09	IBMP	IPMP	SBT	PT	IPT	ET	MT
Method	-24.1	-27.5	-33.1	-36.3	-34.8	-40.5	-35.4	-35.4	-31.9	-31.0	-29.7	-26.3
WATsite	-18.1	-22.0	-17.9	-31.1	-31.1	-31.5	-35.8	-30.6	-34.1	-30.6	-24.2	-16.3
Experimental	-23.1	-28.3	-32.5	-35.6	-38.8	-38.5	-33.9	-35.3	-34.3	-32.6	-29.2	-24.2
MM-GB/SA	-28.5	-33.6	-21.8	-17.8	-32.7	-24.8	-22.8	-33.0	-29.3	-28.8	-25.1	-23.5

Table 6: Binding free energies from hydration site displacement of 12 MUP ligands. Free energies are reported in kJ/mol. For ligands following SBT, structures were obtained by removing specified carbon atoms from the crystal structure of SBT.

This significant correlation is superior to MM-GB/SA results we obtained for the same complexes, where almost no correlation was found (Pearson $R < 0.05$).

Predicted desolvation free energies vs experimental binding free energies

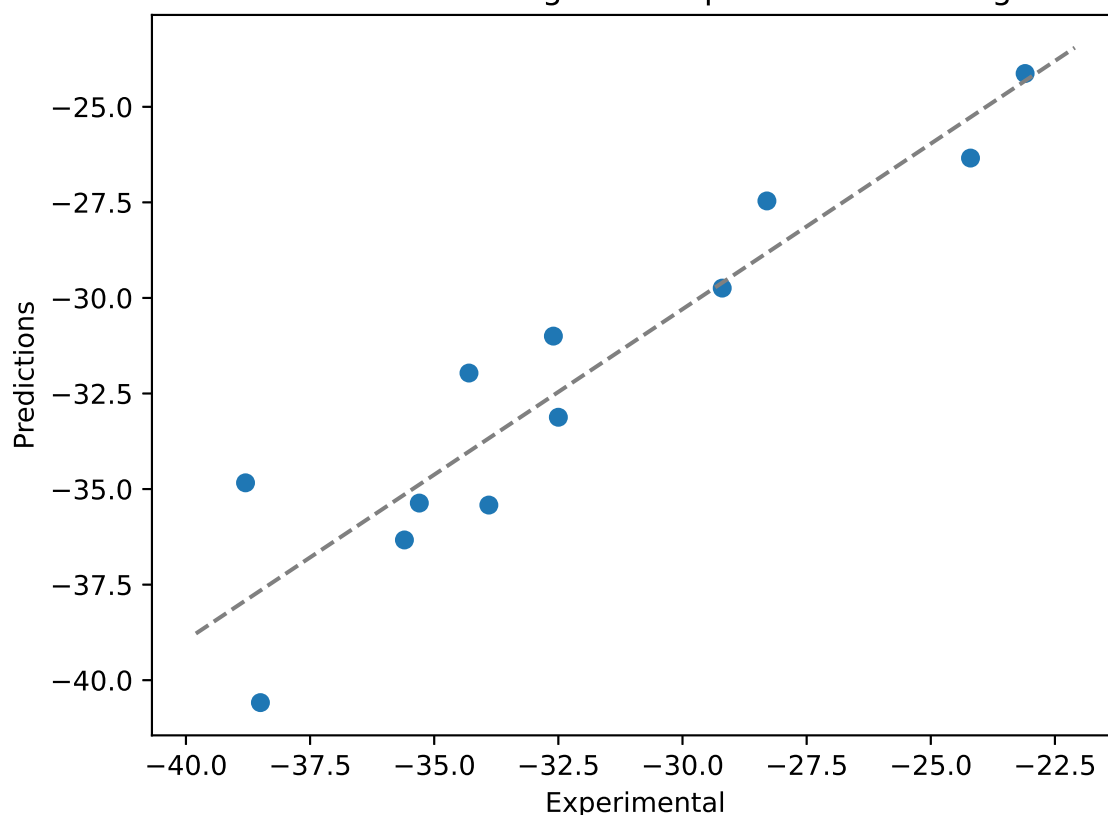


Figure 9: Regression plot comparing predicted desolvation free energy and binding free energy.

5 Conclusion

We introduced a new method for hydration site prediction and thermodynamic profiling based on an equivariant deep neural network trained on a large corpus of MD data. Our results demonstrate that our model is fast, accurate, and robust to chemical and biological perturbations. Other hydration site profiling tools can take several hours for just a single protein conformation due to the expensive explicit-water simulations. However, by leveraging our model we can make predictions on the seconds time scale, enabling high-throughput hydration site prediction and profiling. This is a

crucial advancement to predict hydration sites for flexible proteins in different conformations or for the integration of hydration site prediction into deep learning models for molecular structure prediction. Our results further demonstrated that the model is highly accurate and can reproduce results from molecular dynamics and experimentally resolved structures with high fidelity. Furthermore, thermodynamic predictions from our model showed strong agreement with those obtained from MD and experimentally measured affinities for a series of ligands. We investigated the robustness and generalization of our model since this is a common failure mode seen in deep learning models. Specifically, we evaluated the model under different perturbations to the protein input such as conformational changes and single-point mutations, then confirmed our predictions against the known water locations. The model showed no signs of overfitting and was capable of responding accurately to small changes in the overall protein structure. In summary, our model offers several key advantages over existing hydration site prediction tools. The ability to quickly and accurately predict hydration site locations and thermodynamics has a range of potential applications, from small molecule drug design and lead optimization to peptide and protein design. Our model could also be integrated with other emerging technologies such as deep learning models for co-folding, dynamics, and free energy estimation.

Acknowledgment

The work was partially supported by the Swiss National Science Foundation (Project number: 310030_197629) and the Novartis Research Foundation.

Data availability

- The code for this work is provided here: <https://github.com/lillgroup/HydrationSitePrediction>
- The data is available here: <https://zenodo.org/records/14182834>

References

- [1] Hugh Savage and Alexander Wlodawer. [11] determination of water structure around biomolecules using x-ray and neutron diffraction methods. In *Methods in enzymology*, volume 127, pages 162–183. Elsevier, 1986.
- [2] Bertil Halle. Protein hydration dynamics in solution: a critical survey. *Philosophical Transactions of the Royal Society of London. Series B: Biological Sciences*, 359(1448):1207–1224, 2004.
- [3] Richard Henderson and P Nigel T Unwin. Three-dimensional model of purple membrane obtained by electron microscopy. *Nature*, 257(5521):28–32, 1975.
- [4] Kurt Wüthrich. The way to nmr structures of proteins. *Nature structural biology*, 8(11):923–925, 2001.
- [5] Balázs Zoltán Zsidó, Bayartsetseg Bayarsaikhan, Rita Börzsei, Viktor Szél, Violetta Mohos, and Csaba Hetényi. The advances and limitations of the determination and applications of water structure in molecular engineering. *International Journal of Molecular Sciences*, 24(14):11784, 2023.
- [6] Andriy Kovalenko and Fumio Hirata. Three-dimensional density profiles of water in contact with a solute of arbitrary shape: a rism approach. *Chemical Physics Letters*, 290(1-3):237–244, 1998.
- [7] Andriy Kovalenko and Fumio Hirata. Self-consistent description of a metal–water interface by the kohn–sham density functional theory and the three-dimensional reference interaction site model. *The Journal of chemical physics*, 110(20):10095–10112, 1999.
- [8] Eva Nittinger, Paul Gibbons, Charles Eigenbrot, Doug R Davies, Brigitte Maurer, Christine L Yu, James R Kiefer, Andreas Kuglstatter, Jeremy Murray, Daniel F Ortwine, et al. Water molecules in protein–ligand interfaces. evaluation of software tools and sar comparison. *Journal of computer-aided molecular design*, 33:307–330, 2019.
- [9] William R Pitt and Julia M Goodfellow. Modelling of solvent positions around polar groups in proteins. *Protein Engineering, Design and Selection*, 4(5):531–537, 1991.
- [10] Alexander S Bayden, Demetri T Moustakas, Diane Joseph-McCarthy, and Michelle L Lamb. Evaluating free energies of binding and conservation of crystallographic waters using szmap. *Journal of chemical information and modeling*, 55(8):1552–1565, 2015.
- [11] Jonathan S Mason, Andrea Bortolato, Dahlia R Weiss, Francesca Deflorian, Benjamin Tehan, and Fiona H Marshall. High end gpcr design: crafted ligand design and druggability analysis using protein structure, lipophilic hotspots and explicit water networks. In *Silico Pharmacology*, 1:1–12, 2013.
- [12] Massimo Baroni, Gabriele Cruciani, Simone Sciabola, Francesca Perruccio, and Jonathan S Mason. A common reference framework for analyzing/comparing proteins and ligands. fingerprints for ligands and proteins (flap): theory and application. *Journal of chemical information and modeling*, 47(2):279–294, 2007.
- [13] Gianluca Rossato, Beat Ernst, Angelo Vedani, and Martin Smiesko. Acquaalta: a directional approach to the solvation of ligand–protein complexes. *Journal of chemical information and modeling*, 51(8):1867–1881, 2011.
- [14] Angelo Vedani and David W Huhta. Algorithm for the systematic solvation of proteins based on the directionality of hydrogen bonds. *Journal of the American Chemical Society*, 113(15):5860–5862, 1991.
- [15] Aalt DJ Van Dijk and Alexandre MJJ Bonvin. Solvated docking: introducing water into the modelling of biomolecular complexes. *Bioinformatics*, 22(19):2340–2347, 2006.
- [16] Eva Nittinger, Florian Flachsenberg, Stefan Bietz, Gudrun Lange, Robert Klein, and Matthias Rarey. Placement of water molecules in protein structures: from large-scale evaluations to single-case examples. *Journal of Chemical Information and Modeling*, 58(8):1625–1637, 2018.
- [17] Huynh-Hoa Bui, Alexandra J Schiewe, and Ian S Haworth. Watgen: an algorithm for modeling water networks at protein–protein interfaces. *Journal of computational chemistry*, 28(14):2241–2251, 2007.
- [18] Joost WH Schymkowitz, Frederic Rousseau, Ivo C Martins, Jesper Ferkinghoff-Borg, Francois Stricher, and Luis Serrano. Prediction of water and metal binding sites and their affinities by using the fold-x force field. *Proceedings of the National Academy of Sciences*, 102(29):10147–10152, 2005.
- [19] Akshay Sridhar, Gregory A Ross, and Philip C Biggin. Waterdock 2.0: Water placement prediction for holo-structures with a pymol plugin. *PloS one*, 12(2):e0172743, 2017.
- [20] Bingjie Hu and Markus A Lill. Protein pharmacophore selection using hydration-site analysis. *Journal of chemical information and modeling*, 52(4):1046–1060, 2012.
- [21] Ying Yang, Bingjie Hu, and Markus A Lill. Analysis of factors influencing hydration site prediction based on molecular dynamics simulations. *Journal of Chemical Information and Modeling*, 54(10):2987–2995, 2014.

- [22] Ying Yang and Markus A Lill. Dissecting the influence of protein flexibility on the location and thermodynamic profile of explicit water molecules in protein–ligand binding. *Journal of chemical theory and computation*, 12(9):4578–4592, 2016.
- [23] Yan Li, Yingduo Gao, M Katharine Holloway, and Renxiao Wang. Prediction of the favorable hydration sites in a protein binding pocket and its application to scoring function formulation. *Journal of Chemical Information and Modeling*, 60(9):4359–4375, 2020.
- [24] Jouko J Virtanen, Lee Makowski, Tobin R Sosnick, and Karl F Freed. Modeling the hydration layer around proteins: Hypred. *Biophysical journal*, 99(5):1611–1619, 2010.
- [25] Norbert Jeszenoi, Mónika Bálint, István Horváth, David van der Spoel, and Csaba Hetényi. Exploration of interfacial hydration networks of target–ligand complexes. *Journal of chemical information and modeling*, 56(1):148–158, 2016.
- [26] Norbert Jeszenői, István Horváth, Mónika Bálint, David van der Spoel, and Csaba Hetényi. Mobility-based prediction of hydration structures of protein surfaces. *Bioinformatics*, 31(12):1959–1965, 2015.
- [27] Robert Abel, Tom Young, Ramy Farid, Bruce J Berne, and Richard A Friesner. Role of the active-site solvent in the thermodynamics of factor xa ligand binding. *Journal of the American Chemical Society*, 130(9):2817–2831, 2008.
- [28] Bingjie Hu and Markus A Lill. Watsite: Hydration site prediction program with pymol interface, 2014.
- [29] Ying Yang, Bingjie Hu, and Markus A Lill. Watsite2. 0 with pymol plugin: Hydration site prediction and visualization. *Protein Function Prediction: Methods and Protocols*, pages 123–134, 2017.
- [30] Ying Yang, Matthew R Masters, Amr H Mahmoud, Bingjie Hu, and Markus A Lill. Watsite. user guide a gpu-accelerated hydration site prediction program with pymol plugin. 2018.
- [31] Sangwoo Park and Chaok Seok. Galaxywater-cnn: Prediction of water positions on the protein structure by a 3d-convolutional neural network. *Journal of Chemical Information and Modeling*, 62(13):3157–3168, 2022.
- [32] Andreas Zamanos, George Ioannakis, and Ioannis Z Emiris. Hydraprot: A new deep learning tool for fast and accurate prediction of water molecule positions for protein structures. *Journal of Chemical Information and Modeling*, 64(7):2594–2611, 2024.
- [33] Ahmadreza Ghanbarpour, Amr H Mahmoud, and Markus A Lill. Instantaneous generation of protein hydration properties from static structures. *Communications Chemistry*, 3(1):188, 2020.
- [34] Sangwoo Park. Water position prediction with se (3)-graph neural network. *bioRxiv*, pages 2024–03, 2024.
- [35] Xiaohan Kuang, Zhaoqian Su Su, Yunchao Liu, Xiaobo Lin, Jesse , Tyler Derr, Yinghao Wu, and Jens Meiler. Superwater: Predicting water molecule positions on protein structures by generative ai. *bioRxiv*, pages 2024–11, 2024.
- [36] Florian B Hinz, Amr H Mahmoud, and Markus A Lill. Prediction of molecular field points using se(3)-transformer model. *Machine Learning: Science and Technology*, 4(3):035016, aug 2023.
- [37] F. Pedregosa, G. Varoquaux, A. Gramfort, V. Michel, B. Thirion, O. Grisel, M. Blondel, P. Prettenhofer, R. Weiss, V. Dubourg, J. Vanderplas, A. Passos, D. Cournapeau, M. Brucher, M. Perrot, and E. Duchesnay. Scikit-learn: Machine learning in Python. *Journal of Machine Learning Research*, 12:2825–2830, 2011.
- [38] Petar Veličković, Guillem Cucurull, Arantxa Casanova, Adriana Romero, Pietro Liò, and Yoshua Bengio. Graph attention networks, 2018.
- [39] Matthew R Masters, Amr H Mahmoud, Ying Yang, and Markus A Lill. Efficient and accurate hydration site profiling for enclosed binding sites. *Journal of chemical information and modeling*, 58(11):2183–2188, 2018.
- [40] Renxiao Wang, Xueliang Fang, Yipin Lu, Chao-Yie Yang, and Shaomeng Wang. The pdbbind database: methodologies and updates. *Journal of medicinal chemistry*, 48(12):4111–4119, 2005.
- [41] Minyi Su, Qifan Yang, Yu Du, Guoqin Feng, Zhihai Liu, Yan Li, and Renxiao Wang. Comparative assessment of scoring functions: the casf-2016 update. *Journal of chemical information and modeling*, 59(2):895–913, 2018.
- [42] Martin Steinegger and Johannes Söding. Mmseqs2 enables sensitive protein sequence searching for the analysis of massive data sets. *Nature biotechnology*, 35(11):1026–1028, 2017.
- [43] G Madhavi Sastry, Matvey Adzhigirey, Tyler Day, Ramakrishna Annabhimoju, and Woody Sherman. Protein and ligand preparation: parameters, protocols, and influence on virtual screening enrichments. *Journal of computer-aided molecular design*, 27:221–234, 2013.

- [44] Kevin J Bowers, Edmond Chow, Huafeng Xu, Ron O Dror, Michael P Eastwood, Brent A Gregersen, John L Klepeis, Istvan Kolossvary, Mark A Moraes, Federico D Sacerdoti, et al. Scalable algorithms for molecular dynamics simulations on commodity clusters. In *Proceedings of the 2006 ACM/IEEE Conference on Supercomputing*, pages 84–es, 2006.
- [45] William Humphrey, Andrew Dalke, and Klaus Schulten. Vmd: visual molecular dynamics. *Journal of molecular graphics*, 14(1):33–38, 1996.
- [46] Ying Yang, Amr HA Abdallah, and Markus A Lill. Calculation of thermodynamic properties of bound water molecules. *Computational Drug Discovery and Design*, pages 389–402, 2018.
- [47] Philip J Robinson and Neil J Bulleid. Mechanisms of disulfide bond formation in nascent polypeptides entering the secretory pathway. *Cells*, 9(9):1994, 2020.
- [48] Geqing Wang, Jilong Qin, Anthony D Verderosa, Lilian Hor, Carlos Santos-Martin, Jason J Paxman, Jennifer L Martin, Makrina Totsika, and Begoña Heras. A buried water network modulates the activity of the escherichia coli disulphide catalyst dsba. *Antioxidants*, 12(2):380, 2023.
- [49] Jiashuo Liu, Zheyang Shen, Yue He, Xingxuan Zhang, Renzhe Xu, Han Yu, and Peng Cui. Towards out-of-distribution generalization: A survey. *arXiv preprint arXiv:2108.13624*, 2021.
- [50] Ataur R Katebi and Robert L Jernigan. The critical role of the loops of triosephosphate isomerase for its oligomerization, dynamics, and functionality. *Protein Sci.*, 23(2):213–228, 2014.
- [51] Josh Abramson, Jonas Adler, Jack Dunger, Richard Evans, Tim Green, Alexander Pritzel, Olaf Ronneberger, Lindsay Willmore, Andrew J Ballard, Joshua Bambrick, et al. Accurate structure prediction of biomolecular interactions with alphafold 3. *Nature*, pages 1–3, 2024.
- [52] Rohith Krishna, Jue Wang, Woody Ahern, Pascal Sturmfels, Preetham Venkatesh, Indrek Kalvet, Gyu Rie Lee, Felix S Morey-Burrows, Ivan Anishchenko, Ian R Humphreys, et al. Generalized biomolecular modeling and design with rosettafold all-atom. *Science*, 384(6693):eadl2528, 2024.
- [53] Elisabeth P Carpenter, Konstantinos Beis, Alexander D Cameron, and So Iwata. Overcoming the challenges of membrane protein crystallography. *Current opinion in structural biology*, 18(5):581–586, 2008.
- [54] Ali A Kermani. A guide to membrane protein x-ray crystallography. *The FEBS journal*, 288(20):5788–5804, 2021.
- [55] Lucy A Dunbar, Pranav Patni, Carlos Aguilar, Philomena Mburu, Laura Corns, Helena RR Wells, Sedigheh Delmaghani, Andrew Parker, Stuart Johnson, Debbie Williams, et al. Clarin-2 is essential for hearing by maintaining stereocilia integrity and function. *EMBO Molecular Medicine*, 11(9):e10288, 2019.
- [56] Clara Mendia, Thibault Peineau, Mina Zamani, Chloé Felgerolle, Nawal Yahiaoui, Nele Christophersen, Samantha Papal, Audrey Maudoux, Reza Maroofian, Pranav Patni, et al. Clarin-2 gene supplementation durably preserves hearing in a model of progressive hearing loss. *Molecular Therapy*, 32(3):800–817, 2024.
- [57] Avital Adato, Sarah Vreugde, Tarja Joensuu, Nili Avidan, Riikka Hamalainen, Olga Belenkiy, Tsviya Olender, Batsheva Bonne-Tamir, Edna Ben-Asher, Carmen Espinos, et al. Ush3a transcripts encode clarin-1, a four-transmembrane-domain protein with a possible role in sensory synapses. *European Journal of Human Genetics*, 10(6):339–350, 2002.

A Graphics

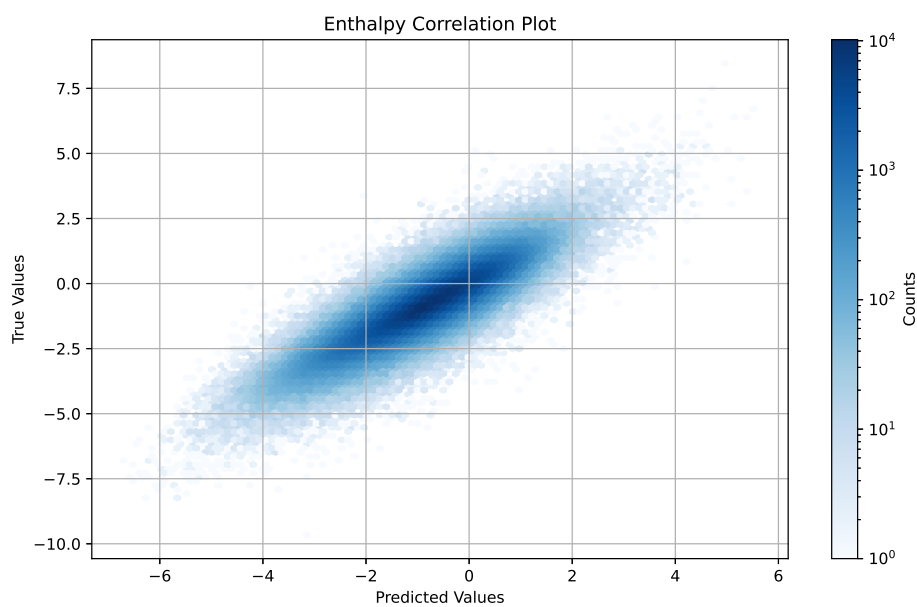


Figure 10: Hexbin plot showing the correlation between the enthalpy predictions and the enthalpy values obtained from WATsite for the train set.

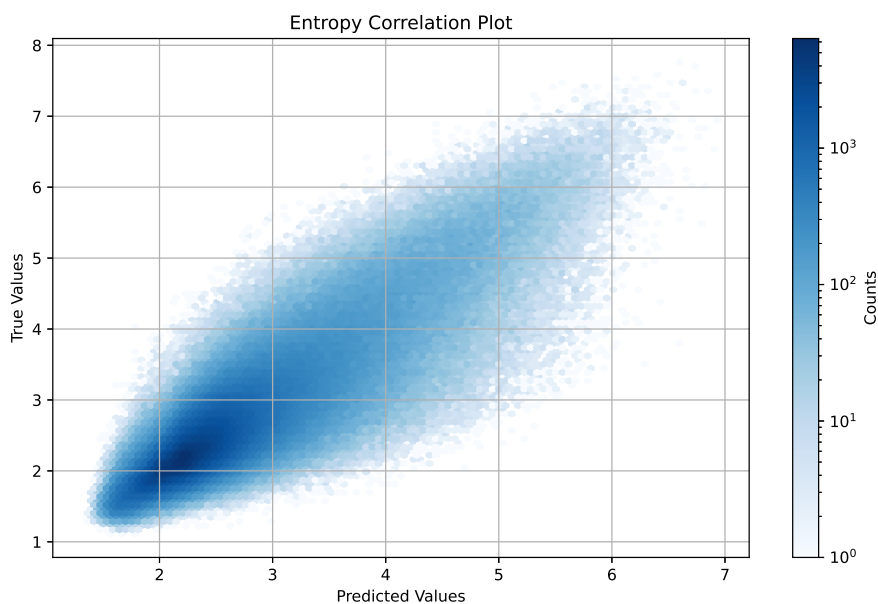


Figure 11: Hexbin plot showing the correlation between the entropy predictions and the entropy values obtained from WATsite for the train set.

B Tables

B.1 Further results on test set

Cutoff	Ground Truth Recovery Rate	Prediction Hit Rate
0.5	37.0%	6.26%
1.0	68.3%	11.5%

Table 7: Ground truth recovery rate and prediction hit rate on xray data

Cutoff	Occupancy				
	[0.5,0.6]	[0.6,0.7]	[0.7,0.8]	[0.8,0.9]	[0.9,1.0]
$r = 0.5$	11.4%	17.6%	22.8%	29.4%	38.5%
$r = 1.0$	20.8%	30.6%	39.8%	50.7%	63.5%
$r = 1.5$	26.6%	38.0%	48.7%	59.4%	74.5%
$r = 2.0$	33.3%	45.6%	56.2%	68.2%	82.2%

Table 8: Second layer waters: Ground truth recovery rate at different occupancy levels

B.2 Results on train set

For reference we provide the results for the training set as well.

Cutoff	Ground Truth Recovery Rate	Prediction Hit Rate
0.5	62.7%	50.2%
1.0	82.1%	66.0%

Table 9: Ground truth recovery rate and prediction hit rate

Cutoff	GTRR first layer	GTRR second layer
0.5	66.2%	16.7%
1.0	86.3%	28.2%

Table 10: Ground truth recovery rate (GTRR) for first and second layer

Cutoff	Occupancy				
	[0.5,0.6]	[0.6,0.7]	[0.7,0.8]	[0.8,0.9]	[0.9,1.0]
$r = 0.5$	45.3%	61.1%	69.2%	74.6%	75.4%
$r = 1.0$	65.1%	81.8%	89.1%	93.0%	93.3%
$r = 1.5$	72.2%	87.5%	93.6%	96.6%	95.9%
$r = 2.0$	76.2%	90.1%	95.4%	97.8%	96.7%

Table 11: Ground truth recovery rate at different occupancy levels

	Occupancy				
	[0.5,0.6]	[0.6,0.7]	[0.7,0.8]	[0.8,0.9]	[0.9,1.0]
Cutoff					
$r = 0.5$	51.7%	64.4%	70.9%	75.3%	75.6%
$r = 1.0$	73.5%	85.8%	90.9%	93.8%	93.4%
$r = 1.5$	80.9%	91.5%	95.3%	97.3%	96.0%
$r = 2.0$	84.5%	93.7%	96.9%	98.3%	96.8%

Table 12: First layer waters: Ground truth recovery rate at different occupancy levels

	Occupancy				
	[0.5,0.6]	[0.6,0.7]	[0.7,0.8]	[0.8,0.9]	[0.9,1.0]
Cutoff					
$r = 0.5$	12.3%	19.8%	27.8%	35.5%	39.6%
$r = 1.0$	21.6%	32.8%	44.8%	54.5%	64.5%
$r = 1.5$	27.3%	39.1%	52.2%	63.1%	72.8%
$r = 1.5$	33.4%	46.1%	58.9%	69.5%	79.2%

Table 13: Second layer waters: Ground truth recovery rate at different occupancy levels

	Entropy	Enthalpy
MSE	0.186	0.279
Correlation	0.867	0.870

Table 14: Correlation and Means Squared Error (MSE) between prediction and ground truth for both entropy and enthalpy on the training set

C Evaluation measures

In order to evaluate the quality of the hydration site coordinate predictions of our model we need to define two evaluation measure: One measuring how many true hydration sites were discovered and a second one setting this into context by measuring how many predictions were reasonable.

Let $m, n \in \mathbb{N}$ and $(a_i)_{i=1}^m \in \mathbb{R}^3$ be the ‘‘ground truth’’ points and $(b_j)_{j=1}^n \in \mathbb{R}^3$ be the ‘‘predictions’’. Let $r \in \mathbb{R}_+$ be the ‘‘cutoff radius’’. Let us agree to the following definitions

$$L_{GTRR}^r := \frac{1}{m} \sum_{i=1}^m \left(1 - \prod_{j=1}^n \mathbb{1}_{]r, \infty[} (\|a_i - b_j\|_2) \right) \quad (8)$$

$$L_{PHR}^r := \frac{1}{n} \sum_{j=1}^n \left(1 - \prod_{i=1}^m \mathbb{1}_{]r, \infty[} (\|a_i - b_j\|_2) \right) \quad (9)$$

We refer to L_{GTRR}^r as the **Ground Truth Recovery Rate (GTRR)** and L_{PHR}^r as the **Prediction Hit Rate (PHR)**.

In words, the *ground truth recovery rate* is the proportion of ground truth elements that have at least one prediction within a radius r . The *prediction hit rate* is the proportion of predictions that are within a radius r of *any* ground truth element.